Water Resources Research

RESEARCH ARTICLE
10.1029/2020WR028408

Upscaling of Solute Plumes in Periodic Porous Media Through a Trajectory-Based Spatial Markov Model

Emanuela Bianchi Janetti[1], **Thomas Sherman**[2], **Gaël Raymond Guédon**[3], **Diogo Bolster**[2], **and Giovanni M. Porta**[1]

[1]Dipartimento di Ingegneria Civile e Ambientale, Politecnico di Milano, Milan, Italy, [2]Department of Civil and Environmental Engineering and Earth Sciences, University of Notre Dame, Notre Dame, IN, USA, [3]Dipartimento di Energia, Politecnico di Milano, Milan, Italy

Key Points:
- A methodology for upscaling multidimensional solute plumes in disordered porous media is proposed
- The proposed approach is suitable for modeling transport of conservative and linearly decaying solute species in a disordered pore space
- The effect of numerical parameters employed in tSMM parameterization on model performance is evaluated

Supporting Information:
- Supporting Information S1

Correspondence to:
E. Bianchi Janetti,
emanuela.bianchi@polimi.it

Citation:
Bianchi Janetti, E., Sherman, T., Guédon, G. R., Bolster, D., & Porta, G. M. (2020). Upscaling of solute plumes in periodic porous media through a trajectory-based spatial Markov model. *Water Resources Research*, *56*, e2020WR028408. https://doi.org/10.1029/2020WR028408

Received 20 JUL 2020
Accepted 4 NOV 2020
Accepted article online 9 NOV 2020

Abstract We propose an approach to upscale solute transport in spatially periodic porous media. Our methodology relies on pore-scale information to predict large-scale transport features, including explicit reconstruction of the solute plume, breakthrough curves at fixed distances, and spatial spreading transverse to the main flow direction. The proposed approach is grounded on the recently proposed trajectory-based spatial Markov model (tSMM), which upscales transport based on information collected from advective-diffusive particle trajectories across one periodic element. In previous works, this model has been applied solely to one-dimensional transport in a single periodic pore geometry. In this work we extend the tSMM to the prediction of multidimensional solute plumes. This is obtained by analyzing the joint space-time probability distribution associated with discrete particles, as yielded by the tSMM. By comparing numerical results from fully resolved simulations and predictions obtained with the tSMM over a wide range of Péclet numbers, we demonstrate that the proposed approach is suitable for modeling transport of conservative and linearly decaying solute species in a realistic pore space and showcase the applicability of the model to predict steady-state solute plumes. Additionally, we evaluate the model performance as a function of numerical parameters employed in the tSMM parameterization.

1. Introduction

Solute transport in porous media is a fundamental problem across many disciplines, including subsurface geological systems and the performance optimization of engineered materials such as filtration membranes. A key challenge in this context is to obtain accurate predictions at spatial scales much larger than the ones associated with individual pores without having to resolve the physical and chemical processes taking place within complex pore spaces. This is achieved by upscaled formulations that embed pore-scale features into effective parameters and therefore can be employed to predict large-scale behaviors. To this end, a classical approach is resorting to a continuum-scale advection-dispersion equation (ADE) (Cheng & Bear, 2016; Scheidegger, 1954). In such a formulation mechanical dispersion induced by pore-scale velocity gradients is modeled through a Fickian-like dispersion term, parameterized via a fourth-rank dispersivity tensor. The definition of the dispersivity tensor purely based on pore-scale properties presents significant challenges. From a theoretical perspective, the solution of three closure problems is required to fully parameterize solute transport based on pore-scale information through volume averaging (Valdés-Parada et al., 2016). These separate closures are necessary to isolate and characterize the separate effects of diffusion and advection on transport. However, even such a detailed approach may not yield reliable predictions due to a lack of separation of scales, violating the assumptions required by the volume averaging method. In such a case, non-Fickian transport features emerge, particularly at relatively short times and distances (Berkowitz et al., 2006; Salles et al., 1992). Formally, these effects can still be represented with Eulerian nonlocal (integro-differential) models. In principle these models can be derived by applying upscaling approaches, such as volume averaging, that can relate pore-scale geometry and fluid velocities with the emerging transport dynamics through a set of closure differential equations (Wood & Valdés-Parada, 2013). However, it is often found that resorting to such approaches leads to formidable mathematical and numerical complexity (Davit et al., 2012; Porta et al., 2016), which is associated with (i) the numerical resolution of various closure problems and (ii) the approximation of integro-differential equations to obtain the desired large-scale outputs.

A specific problem in the context of solute transport upscaling is posed by the modeling of solute plumes, which corresponds to the explicit spatial reconstruction of the solute spatial spread at a given time, or at steady state (i.e., under steady-state boundary conditions, such as continuous injection). For instance, the analysis of transverse spreading and mixing of steady-state solute plumes has great practical relevance in bioremediation and reactive transport scenarios at field and laboratory scales (Cirpka & Valocchi, 2007; Chiogna et al., 2010; Tang et al., 2015). In these applications the target process is the spreading and mixing of a solute in the direction transverse to a steady flow field characterized by a prevalent direction. Following classical ADE-based descriptions, transport in the transverse direction is typically modeled by introducing a dispersivity parameter. This standard definition typically considers dispersion to be uniquely proportional to advective velocity (Scheidegger, 1954). This formulation was successfully employed, for example, to interpret transport and mixing in microfluidic systems characterized by relatively simple geometries (Willingham et al., 2008). However, studies performed in the last decade have demonstrated the impact of molecular diffusion on transverse dispersion through experiments and numerical simulations (Chiogna et al., 2010; Muniruzzaman & Rolle, 2015; Rolle et al., 2012; Ye et al., 2016). Such results can be qualitatively linked with analytical and numerical studies showing that the dispersion tensor becomes asymmetric in advection-dominated scenarios (Auriault et al., 2010; Pride et al., 2017). These studies show that full parameterization of the dispersion tensor can become a troublesome task, particularly in media characterized by a complex and multiscale pore structure. Additional levels of complexity are introduced when reactive processes are also considered on top of pore-scale advective-diffusive transport.

Over the last decade it has been recognized that pore-to-continuum upscaling of solute transport can often be conveniently obtained by considering solute velocities (or associated travel times) over fixed spatial increments by means of a Markov chain. This led to the formulation of various flavors of so-called spatial Markov models (SMMs) (e.g., Kang et al., 2014; Le Borgne et al., 2011; Puyguiraud et al., 2019; Sherman, Bianchi Janetti, et al., 2020). The SMM is based on the calculation of the travel time across a fixed distance and a one-step correlation existing between successive travel times. By including correlation the SMM is able to employ information available on a limited portion of the system to predict transport across much larger distances. Notably, such an approach is effective in the presence of advection-dominated scenarios that become challenging to upscale with classical Eulerian approaches. The advantages of employing a spatial Markov approach to obtain the solute breakthrough curve (or first passage time) at a given longitudinal distance has been demonstrated in a number of previous works, relying on both numerical and laboratory-scale experimental data sets (e.g., Bolster et al., 2014; Le Borgne et al., 2011; Sherman, Bianchi Janetti, et al., 2020; Sherman et al., 2018). Several recent works have discussed methodologies that employ Lagrangian SMM-like approaches to predict solute particles' space-time locations at various scales of observations (Russian et al., 2016; Wright et al., 2019). Yet, to the best of our knowledge, this approach has not been applied to the explicit space-time reconstruction of solute plumes starting from pore-scale properties. In this work, we pursue this objective with the aim of opening new pathways for the application of SMM approaches to transport in porous media at laboratory and field scales. To achieve this goal, our work starts from that of Sund et al. (2017), Sherman et al. (2019), and Most et al. (2019) where a trajectory-based SMM (here labeled tSMM) was formulated. The methodology relies on a set of numerically simulated Lagrangian trajectories obtained for a single unit cell of the porous medium, which is then used to predict transport across much larger distances. The approach has been applied so far to the simulation of transport, mixing and surface reactions across a periodic pore with a highly idealized geometry. From a methodological standpoint, these previous implementations of the tSMM are unable to (i) simulate transport in complex porous media and (ii) model transverse spreading of solute plumes which is highly relevant in the situations described above. The present work aims to overcome these limitations. In particular, the specific objectives of this contribution are to (i) extend the tSMM to the upscaling of transient and/or steady-state solute transport in the longitudinal and transverse direction and (ii) yield an efficient, accurate and computationally affordable representation of the ensuing multidimensional solute plumes. As such, our approach paves the way for novel fields of application for the tSMM by extending its applicability to problems displaying various spatial (one-dimensional and multidimensional) and temporal characteristics (steady and unsteady). This latter point is particularly challenging because the simulation of steady-state transport with Lagrangian methodologies typically entails very large computational costs, as well as the need to implement specific methods to impose boundary conditions that are consistent with those considered in classical Eulerian models based on partial differential equations (Koch & Nowak, 2014; Sole-Mari et al., 2019).

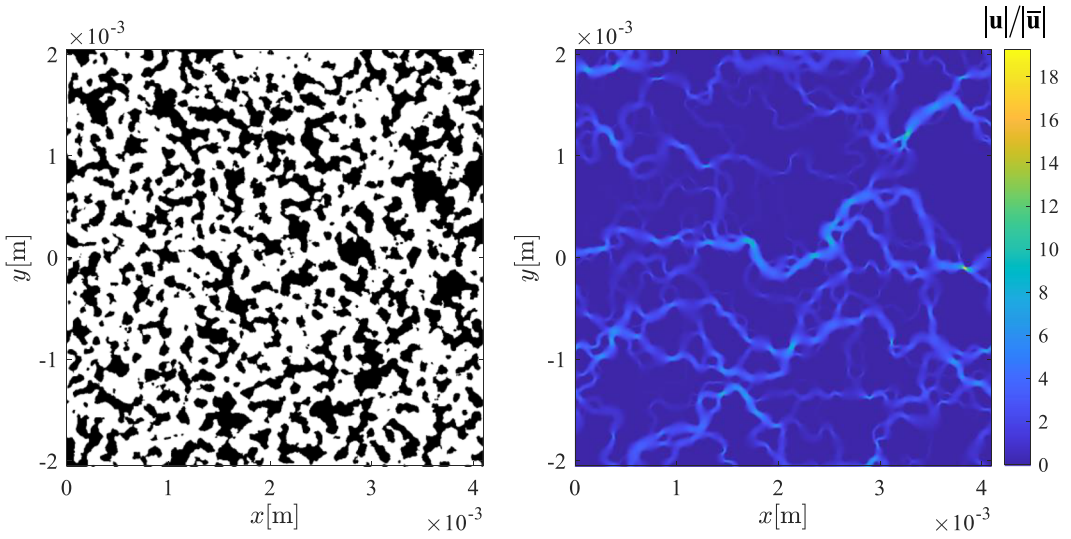

Figure 1. Geometry (left) and normalized velocity magnitude $|\mathbf{u}|/\overline{|\mathbf{u}|}$ (right) in the unit cell.

To accomplish these goals, we consider a periodic medium showing a disordered periodic geometry. Periodicity is imposed in agreement with numerous theoretical upscaling approaches applied in porous media and are relevant to engineering systems across a wide range of applications (Gebäck & Heintz, 2019; Kim et al., 2013; Municchi & Icardi, 2020; Schmuck & Berg, 2014).

2. Methodology

2.1. Pore-Scale Setting

We consider transport of a passive solute in a periodic two-dimensional porous medium. The medium is composed of a collection of periodic unit cells, whose geometry is represented in Figure 1. The unit cell is artificially created using a stochastic generation procedure as detailed in Sherman, Bianchi Janetti, et al. (2020), Smolarkiewicz and Winter (2010), and Hyman and Winter (2014). The cell properties are reported in Table 1. We assume here to deal with a semi-infinite periodic porous domain, that is, $x \in [0, \infty)$ and $y \in (-\infty, +\infty)$. Because the medium is composed by an infinite number of identical cells, for convenience we define

$$\hat{x} = x - L_x \text{floor}\left(\frac{x}{L_x}\right), \quad \hat{y} = y + \frac{L_y}{2} - L_y \text{floor}\left(\frac{y}{L_y} + \frac{1}{2}\right) \tag{1}$$

as a coordinate system referenced to the unit cell, $\hat{x} \in [0, L_x]$ and $\hat{y} \in [0, L_y]$, where L_x and L_y define the dimensions of the unit cell in the x and y directions, respectively.

The cell is discretized into square pixels of side $\Delta = 2 \times 10^{-6}$ m, which for our example results in a unit cell composed of 2,048 × 2,048 pixels. The solid and fluid phases are identified by an indicator field I, with $I = 1$ associated with pore space and $I = 0$ with solid pixels. The correlation length of the indicator field I is taken as a representative length scale for the pore space and is denoted as ℓ_S. Transport is described by the standard advection-diffusion equation with no flux boundary conditions at the solid-fluid interface:

$$\begin{aligned} \tfrac{\partial C(\mathbf{x},t)}{\partial t} + \boldsymbol{\nabla} \cdot [\mathbf{u}(\mathbf{x}) C(\mathbf{x},t)] &= \boldsymbol{\nabla} \cdot [D \boldsymbol{\nabla} C(\mathbf{x},t)] \qquad \forall \mathbf{x} \in \Gamma_{fluid}, t > t_0 \\ D \tfrac{\partial C(\mathbf{x},t)}{\partial n} &= 0 \qquad \forall \mathbf{x} \in \Sigma_{surface}, t > t_0 \\ C(\mathbf{x}, t_0) &= C_0, \end{aligned} \tag{2}$$

Table 1
Geometrical Characteristics of the Unit Cell

Porosity	L_x (m)	L_y (m)	Δ (m)	ℓ_S (m)
0.631	4.096×10^{-3}	4.096×10^{-3}	2×10^{-6}	1×10^{-4}

Note. L_x, L_y, Δ and ℓ_S indicate, respectively, the dimensions of the unit cell, the spatial discretization along x and y directions, and the representative length scale of the system.

where $\mathbf{u} = [u, v]$ is the fluid velocity, C is solute concentration, D is the diffusion coefficient, and C_0 is the initial concentration distribution. The velocity $\mathbf{u}$ is obtained by numerically solving the Navier-Stokes equations with OpenFOAM®, release v1712 (OpenCFD Limited, 2017) and diffusion coefficient is assumed to be known and constant. We impose a uniform pressure gradient along the x direction, labeling x an y as longitudinal and transverse directions, respectively. The velocity is computed assuming periodic boundary conditions on the top-bottom cell boundaries and the no slip condition on the fluid-solid interface. The Péclet number associated with transport is calculated as $Pe = U\ell_S/D$, where U is the average fluid velocity along the x direction over the whole fluid domain. In our simulation we set $D = 10^{-9}$ m^2/s and we adjust Pe by setting U to the desired value. Note that this is acceptable as our simulations are in a Stokes regime, where inertial effects are negligible with respect to viscous ones. Transport is solved numerically using a Lagrangian particle-based random walk method, where the solute plume is discretized into a finite number of N particles. Each particle displaces according to

$$\begin{aligned} x_i^{n+1} &= x_i^n + u_i dt + \xi_i \sqrt{2Ddt} \\ y_i^{n+1} &= y_i^n + v_i dt + \eta_i \sqrt{2Ddt} \end{aligned} \qquad i = 1, \ldots, N, \tag{3}$$

where dt is a time step that is constant, ξ_i, η_i are independent identically distributed random numbers drawn from normal distributions with zero mean and unit variance. We define a reference time step dt^* according to the following criterion $|\mathbf{d}_{max}| \leq 0.5\Delta$ where

$$|\mathbf{d}_{max}| = \max\left(|\mathbf{u}|\right) dt + 2\sqrt{2Ddt^*} \tag{4}$$

is an estimate of the maximum displacement. No flux boundary conditions at the fluid-solid boundary are imposed as elastic reflections (see the supporting information for additional details). We note here that the unit cell porosity, as well as the correlation between void and solids are fixed as input parameters of the generation methodology and may have an impact on the resulting flow field and consequently on the solution of transport equation (see Equation 3). For example, imposing a smaller porosity will promote channeling and, in turn, the concentration of trajectories along similar paths in the periodic cell. In this case rare events will likely dominate diffusion in cavities and dead end pores, resulting in tailing and solute delays. The analysis of the influence of the parameters used for the stochastic generation of the unit cell can be performed in a parametric study or in the context of multiple Monte Carlo pore space realizations. However, all these aspects are not within the objectives of the present work and will not be discussed further here.

2.2. SMM

We upscale transport using the framework of the tSMM proposed in Sund et al. (2017). The methodology is based upon pore-scale transport trajectories and their associated travel times. In the following, we first describe the pore-scale trajectories simulations and then how these are used to parameterize the tSMM.

2.2.1. Pore-Scale Trajectories

Parameterization of the model is grounded on the pore-scale simulation of a set $S = \{s_1, \ldots, s_{N_s}\}$ of N_s advective-diffusive trajectories, for a specific Pe. These particle trajectories are simulated by solving Equation 3 across a single cell in the longitudinal direction, that is, between the inlet location $x = 0$ and the outlet location $x = L_x$. Figure 2 represents a sample of 100 trajectories across the considered unit cell selected from a flux weighted initial condition and setting initial location of particles distributed along the entire unit cell cross section. The comparison between the two considered cases allows for identification of the effects of diffusion on the pore-scale trajectory paths. Although there is a factor of 10 difference in terms of Pe between the two cases, the trajectories appear very similar at first sight. Differences are noted only after close inspection of the details of the trajectories paths, where it is apparent that for $Pe = 100$ particles explore a wider portion of the pore space than for $Pe = 1{,}000$ (cf. Figures 2b and 2d). These apparently small differences will have a definite impact on the response of the system. In other words, even if the input-output connectivity is broadly similar in the two cases and is constrained by the geometry of the cell, the emerging transport behavior will be quite different and is sharply influenced by Pe, i.e., by the physics of the transport process, as will be shown in section 3. We observe that for diffusion-dominated cases ($Pe \leq O(1)$) the trajectories would display a different pattern and explore the geometry cell much more uniformly than shown in Figure 2. This case is however not explored in this contribution, as upscaling there is typically more straightforward and our focus is on advection-dominated cases. For each trajectory s_i we record the travel time τ needed to travel across a distance L_x in the longitudinal direction and the y positions (y_{in}, y_{out}) of

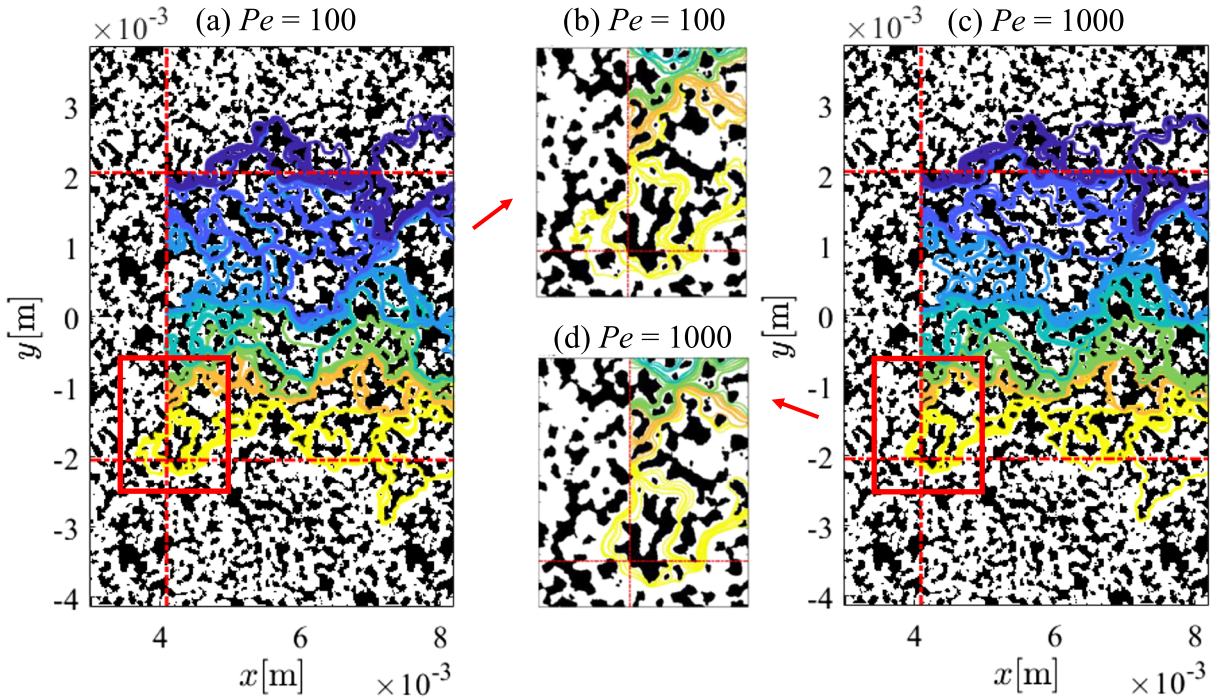

Figure 2. Sample of 100 trajectories employed for model parameterization for (a and b) $Pe = 100$ and (c and d) $Pe = 1{,}000$. Dashed red lines indicate the unit cell boundaries, and the trajectories are binned in different colors as a function of the y_{in} location. The two middle panels represent a zoom on the region highlighted in red for the two cases.

the particle at the inlet and outlet as the particle enters and exits the domain. Particles are injected at locations $x = 0, y_{in} \in [-L_y/2, L_y/2]$. Particles may cross into adjacent cells along the y direction, but due to the periodicity of the cell geometry, each location y_{out} can be mapped to a corresponding $\hat{y}_{out}$ using Equation 1. Therefore, the coordinate $y_{out}(s_i)$ can be determined as $y_{out}(s_i) = \hat{y}_{out}(s_i) + \Delta_C(s_i)L_y$, where $\Delta_C(s_i)$ is an integer that indicates the net number of cell transitions in the transverse direction observed for a given s_i trajectory path. We can then compute $\Delta y(s_i) = y_{out}(s_i) - y_{in}(s_i)$. The trajectories are subdivided into N_B equiprobable bins that are assigned by considering the starting locations $y_{in}(s_i)$ in ascending order. This implicitly defines a discretization of the $\hat{y}$ axis in terms of the binning of the trajectories. To exemplify this binning, the trajectories in Figure 2 are subdivided into 10 bins, indicated by different colors. The trajectories s_i consider all simulated pathways between the locations $x = 0, y_{in} \in [-L/2, L_y/2]$ and $x = L_x, y_{out} \in (-\infty, +\infty)$. We observe that some trajectories may even travel backward along x close to the inlet section before traveling downstream, as indicated in the highlighted parts in Figure 2. These effects are present for both considered Pe and are likely to be emphasized in a two dimensional setting if compared to a three-dimensional one with similar characteristics.

2.2.2. The tSMM Parameterization

The information collected in the parameterization step is then used to build the following tSMM:

$$\begin{aligned} x_i^{k+1} &= (k+1)L_x \\ y_i^{k+1} &= y_i^k + \Delta y\left[s_i^k | \hat{y}_{out}(s_i^{k-1})\right] \\ t_i^{k+1} &= t_i^k + \tau\left[s_i^k | \hat{y}_{out}(s_i^{k-1})\right] \end{aligned} \tag{5}$$

where both y_i^{k+1} and t_i^{k+1} are determined through a Markov chain, which is related to the transverse location assigned to the particle in the periodic cell during successive steps k, leveraging the information given by the trajectories in s_i. The innovative feature of the model in Equation 5 with respect to previous implementations (Sherman, Bianchi Janetti, et al., 2020; Sund et al., 2017) is that it allows for predictions of transverse spreading over successive Markov steps. This is achieved by considering y as a continuous variable; that is, the Markov chain has a longitudinal fixed spatial step L_x, while transport along y is considered through the $\Delta y(s_i)$ obtained from the trajectories s_i recorded during the parameterization stage. In essence, at the beginning of the simulation (step $k = 0$) each particle i is assigned to an initial location y_i^0 corresponding to a

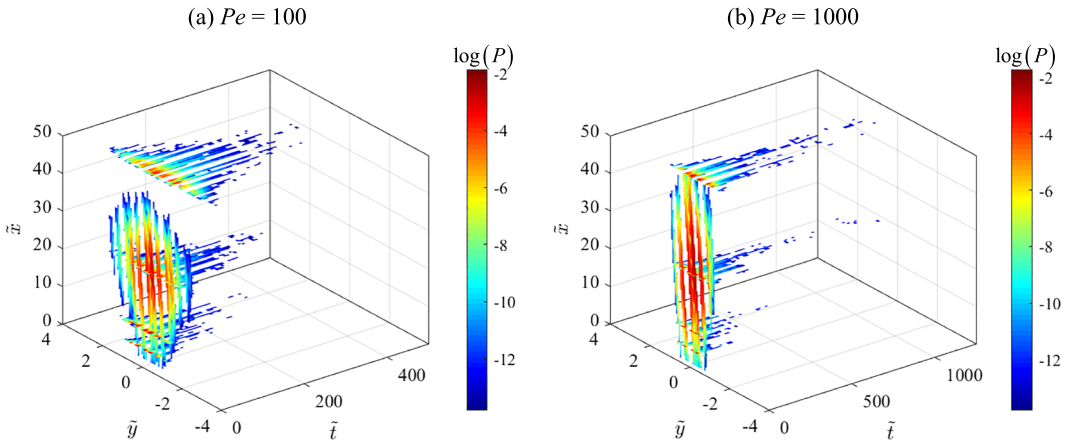

Figure 3. Conditional joint distributions $P(\tilde{t}, \tilde{y}|\tilde{x})$ for $\tilde{x} = 5$, 10, 25, and 50 and $P(\tilde{x}, \tilde{y}|\tilde{t})$ for $\tilde{t} = 20$ predicted by the tSMM considering (a) $Pe = 100$ and (b) $Pe = 1{,}000$.

selected initial or boundary condition (e.g., flux weighted or uniform distribution on the inlet boundary). From this information we select a trajectory s_i^1, randomly sampling from those whose $y_{in}(s_i)$ lies in the same bin interval as y_i^0. By selecting the trajectory, we also obtain a given travel time $\tau(s_i^1)$ and transverse displacement $\Delta y(s_i^1)$, from which we evaluate $\hat{y}_{out}(s_i^1)$. The latter can be then used to select a new trajectory s_i^2 for the next transition and the procedure can then be repeated for any arbitrary step number $k > 0$.

2.3. Model Outputs

To analyze the outputs of our tSMM model, our analysis relies on the following dimensionless space-time coordinates

$$\tilde{x} = \frac{x^k}{L}, \qquad \tilde{y} = \frac{y_c}{L}, \qquad \tilde{t} = \frac{tU}{L} \tag{6}$$

where $L = L_x = L_y$, x^k corresponds to the longitudinal spatial coordinate of kth Markov step (see Equation 5) and $y_c(x) = y(x) - \bar{y}(x)$, that is, is the transverse location centered with respect to the average transverse position $\bar{y}(x)$ observed at a given x. The value of $\bar{y}(x)$ is not constant with x because the average transverse velocity component is not exactly equal to 0. While this component is only approximately 1% of the longitudinal mean velocity U, it still induces plume migration along y after a number of cells.

The key output of the tSMM is the joint probability distribution $P(\tilde{x}, \tilde{y}, \tilde{t})$. In this distribution, the variable $\tilde{x}$ can only assume discrete values, while the $\tilde{y}, \tilde{t}$ are continuous.

Physically meaningful information related to the plume can then be extracted from this joint probability by considering conditional and marginal distributions. In our analysis we will consider the conditional distributions $P(\tilde{t}, \tilde{y}|\tilde{x})$ for a given dimensionless downstream distance $\tilde{x}$, or $P(\tilde{x}, \tilde{y}|\tilde{t})$ for a given dimensionless time, $\tilde{t}$. Examples of these conditional distributions $P(\tilde{t}, \tilde{y}|\tilde{x})$ for $\tilde{x} = 5$, 10, 25, and 50 and $P(\tilde{x}, \tilde{y}|\tilde{t})$ for $\tilde{t} = 20$ obtained from the tSMM are shown in Figures 3a and 3b for $Pe = 100$ and 1,000, respectively.

In addition, we consider the marginal probability distributions $P(\tilde{x}, \tilde{y})$, and $P(\tilde{t}|\tilde{x})$, $P(\tilde{y}|\tilde{x})$ conditional to a given dimensionless downstream distance. These distributions have a clear physical meaning: the marginal distribution $P(\tilde{x}, \tilde{y})$ represents the steady-state distribution of the particle plume, while $P(\tilde{t}|\tilde{x})$ corresponds to the breakthrough curve, that is, the first passage time probability distribution at distance $\tilde{x}$. Finally, the probability distribution $P(\tilde{y}|\tilde{x})$ provides the probability distribution associated with transverse position at a control plane and is related solely to transport in the transverse direction.

To produce benchmark data against which to test the tSMM we run a random walk direct numerical simulation (DNS) using transport Equation 3 considering a medium composed of the collection of 50 periodic cells whose properties are described in Table 1. The accuracy of the tSMM defined in section 2.2 will be tested by comparing the above mentioned probability distributions with their analogs obtained from the DNS. For

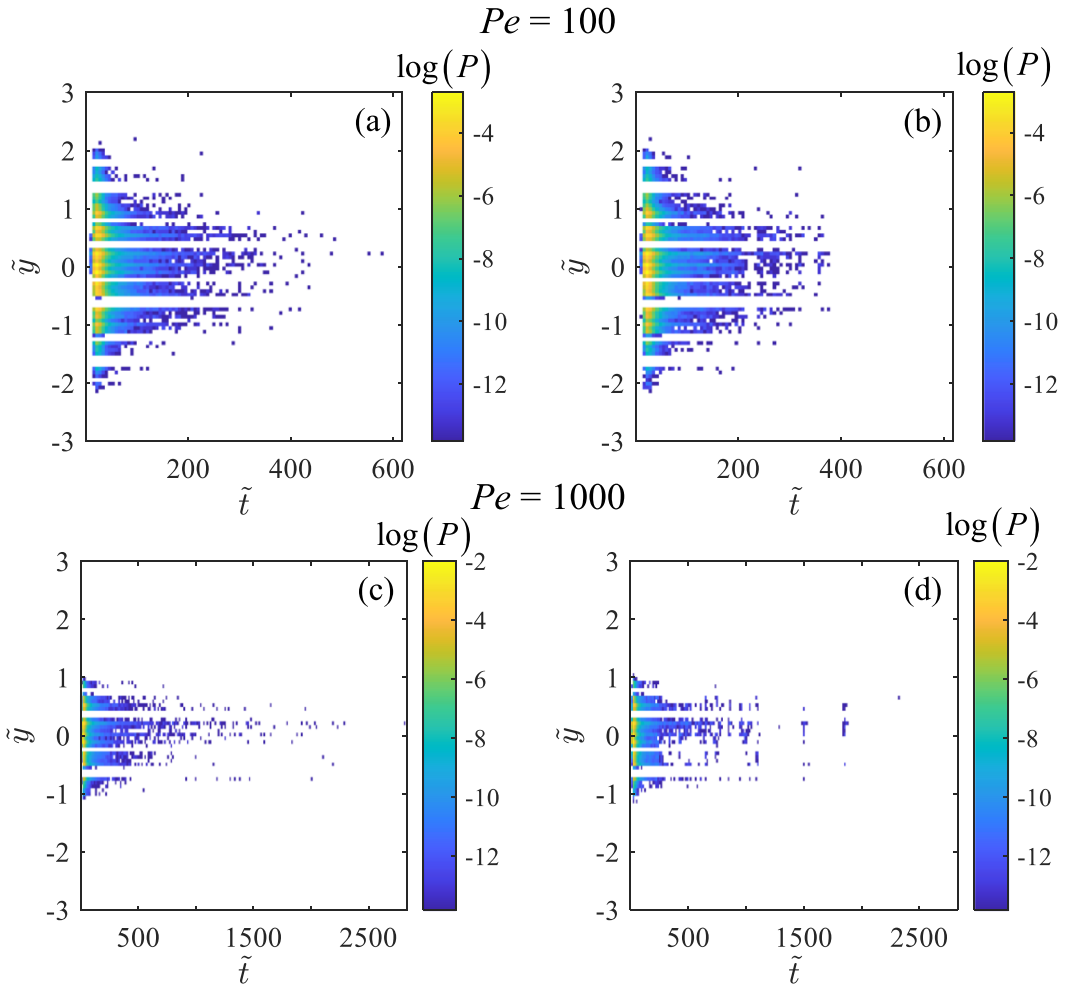

Figure 4. Conditional joint distributions $P(\tilde{t}, \tilde{y}|\tilde{x})$ for $\tilde{x} = 25$ and $Pe = 100$ obtained with (a) DNS and (b) tSMM and for $Pe = 1{,}000$ predicted by (c) DNS and (d) tSMM.

each of the above defined distributions we provide a quantitative evaluation of the mismatch between DNS and tSMM using the Hellinger distance (Hellinger, 1909):

$$HD[F_1, F_2] = \frac{1}{\sqrt{2}} \sqrt{\sum_{i=1}^{N} \left(\sqrt{f_{1,i}} - \sqrt{f_{2,i}} \right)^2}, \tag{7}$$

where F_1 is any of the above-mentioned marginal or conditional distributions predicted by DNS and F_2 corresponds to its counterpart obtained with the tSMM. These distributions are approximated through N discrete bins, and $f_{1,i}$ and $f_{2,i}$ are the values of the distributions in the i^{th} bin.

The *HD* metric quantifies the distance between two probability measures, and it is a proper distance metric in the mathematical sense, by satisfying the properties of nonnegativity, symmetry, and triangle inequality. *HD* is also bounded between 0 and 1, where 0 means that the two distributions are indiscernible and 1 that they are maximally distant. As an additional advantage with respect to other metrics, e.g., the Kullback-Leibler divergence (Kullback & Leibler, 1951), this metric can be employed also if the two distributions have a different support.

3. Results

First, we show results obtained considering parameterization of the tSMM with $N_s = 10^6$, $N_B = 100$, $dt^* = 10^{-5}$ s, and 10^{-6} s for $Pe = 100$ and $Pe = 1{,}000$, respectively. The time step dt^* indicates the values of dt evaluated according to Equation 4. Then, in section 3.3 we analyze the impact of parameters N_B and dt on

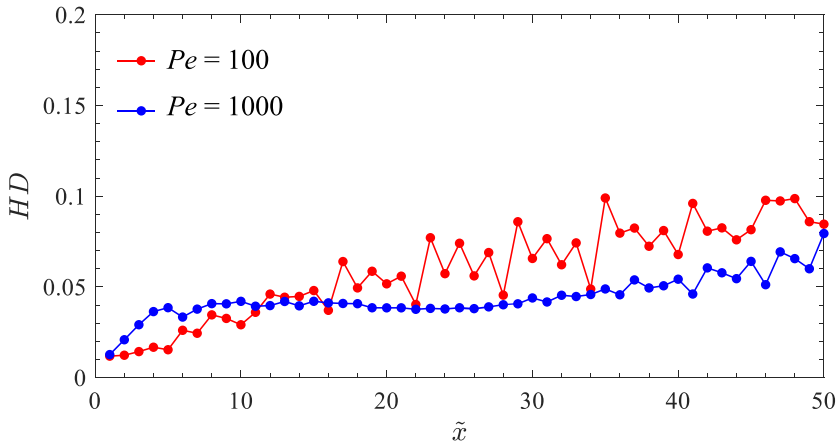

Figure 5. $HD[P_{DNS}(\tilde{y},\tilde{t}|\tilde{x});P_{tSMM}(\tilde{y},\tilde{t}|\tilde{x})]$ as a function of the downstream location $\tilde{x}$ for $Pe = 100$ (red) and 1,000 (blue).

the accuracy of the tSMM. For all cases, including the DNS reference simulation and tSMM, we impose a flux weighted boundary conditions. Note that in the reference DNS simulation the dt parameter is kept constant and equal to dt^*.

3.1. Model Performance as a Function of *Pe*

The tSMM is able to replicate the shape of the reference conditional distribution $P(\tilde{t},\tilde{y}|\tilde{x})$ obtained from the DNS for both investigated Péclet numbers. Figure 4a shows the joint distribution $P(\tilde{t},\tilde{y}|\tilde{x})$ for $\tilde{x} = 25$ and $Pe = 100$ from the high-resolution DNS and corresponding results obtained with the tSMM (Figure 4b). The agreement between the two solutions is significant for all transverse coordinates, $\tilde{y}$, and dimensionless travel times, $\tilde{t}$. Analogous results are obtained for $Pe = 1{,}000$ (see Figures 4c and 4d) and for all other investigated Markov steps (not shown). For both Pe values the maximum value of the probability distributions is found at $\tilde{y} \approx 0$. Note that $\tilde{y}$ locations associated with zero probability across the whole time window correspond to the occurrence of solid along the considered transverse section.

To quantify the accuracy of the tSMM outputs with respect to the reference DNS, Figure 5 shows the metric $HD[P_{DNS}(\tilde{y},\tilde{t}|\tilde{x});P_{tSMM}(\tilde{y},\tilde{t}|\tilde{x})]$ defined in Equation 7 for both investigated Pe numbers and all Markov steps. We note that the distance between the DNS and the tSMM distributions slightly increases with $\tilde{x}$ and is generally larger for $Pe = 100$ than for $Pe = 1{,}000$. This result is likely due to the fact that the effect of noise in low probability values increases with the strength of diffusion. Fluctuations related to $Pe = 100$ are associated with the increased noise associated with the increasing effect of diffusion (for decreasing Pe number), with noise becoming significant in the less densely populated positions far from the plume center (see Figure 4).

Figure 6 depicts conditional joint distribution $P(\tilde{x},\tilde{y}|\tilde{t})$ for $\tilde{t} = 20$, corresponding to the time-dependent solute plume. DNS and tSMM predictions are shown for $Pe = 100$ (see Figures 6a and 6b) and for $Pe = 1{,}000$ (see Figures 6c and 6d). Again, the tSMM is able to capture all essential features displayed by the fully resolved simulations. Note that tSMM allows for predictions of the evolution of the plume in the longitudinal and transverse directions employing a significantly smaller computational effort than the DNS. The total computational time required for tSMM is obtained as the sum of the time required for (i) one periodic cell DNS calculation (needed for tSMM parameterization) and (ii) the solution of Equation 5 for the considered Markov steps. As an example, the total computational time for running the tSMM is approximately 2.0% of that one needed for the DNS results when considering 50 Markov steps for $Pe = 100$ and 1.8% for $Pe = 1{,}000$. Note that this percentage decreases for simulation across higher numbers of unit cells (i.e., the computational gain increases with the dimension of the system of interest). This is related to the fact that, as specified above, the parameterization of the tSMM requires as initial step a DNS simulation over a single periodic cell, which is the most computationally intensive part of the procedure. Conversely, the computational gain for fixed dimension of the system only slightly decreases with decreasing Pe, because the time required for the unit cell DNS employed for the tSMM parameterization increases proportionally to the time required for the DNS over the whole system. Additional details about computational time are included in the supporting information.

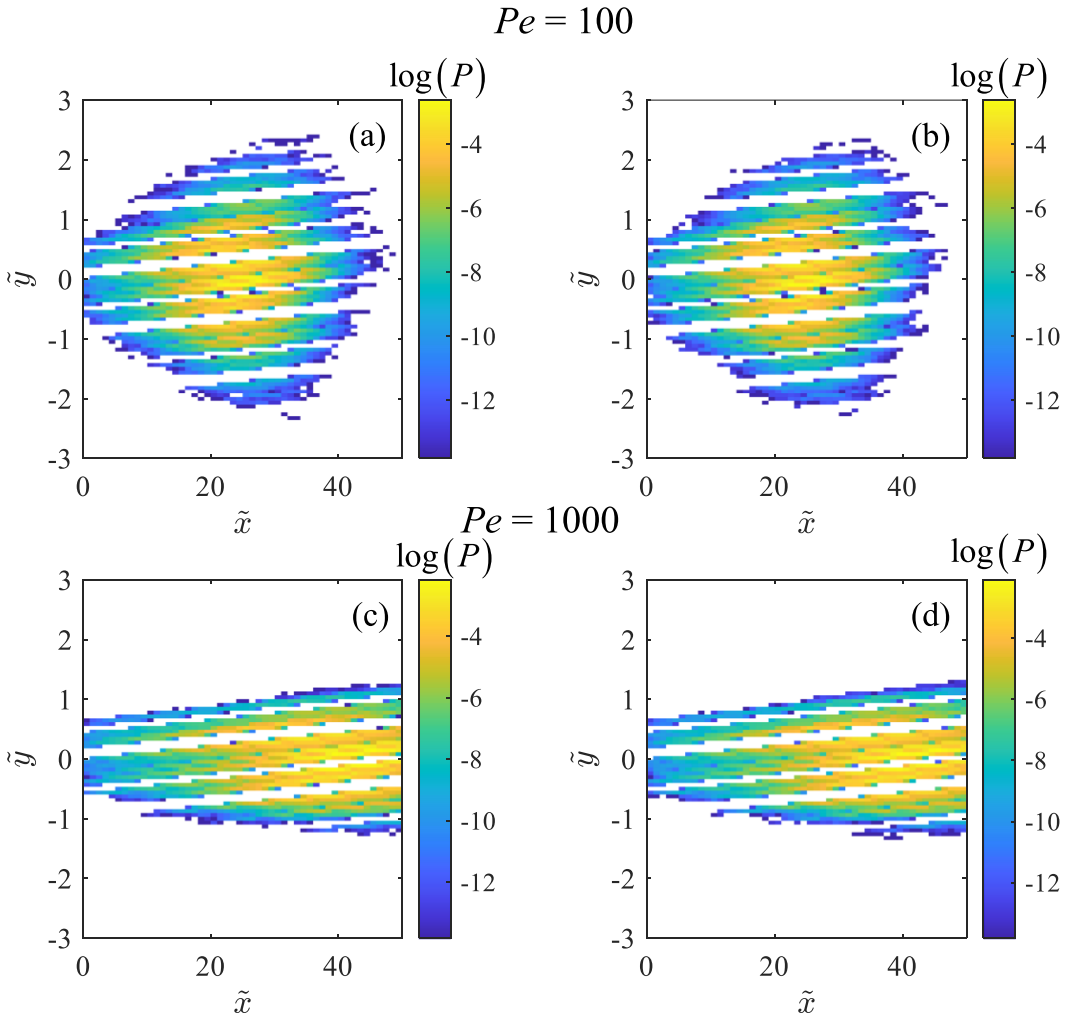

Figure 6. Conditional distributions $P(\tilde{x}, \tilde{y}|\tilde{t})$ for $\tilde{t} = 20$ and $Pe = 100$ obtained with (a) DNS (b) tSMM and for $Pe = 1{,}000$ predicted by (c) DNS and (d) tSMM.

The marginal distributions $P(\tilde{x}, \tilde{y})$ are depicted in Figures 7a and 7b for $Pe = 100$ and 1,000, respectively. As mentioned above, these distributions identify the steady-state plume for a nonreactive solute. These distributions are here obtained at no additional computational cost with respect to the transient case, which for a DNS would not be the case and significant additional cost would be required. These results are obtained considering a flux weighted injection of particles along the entire cross section of the unit cell. Note that the form of system (5) does not change if we consider different types of injection conditions. Different injection conditions simply require to set up the Markov Chain in Equation 5 with different starting locations y_i^0. These different simulations can then rely on the same set of trajectories for parameterization and would be associated with very low computational costs (see the last column of Table S1) if compared with a pore-scale DNS. For illustrative purposes, we perform an additional tSMM simulation where the injection takes place in a point rather than along a whole inlet section of the periodic cell and the ensuing results are shown in the supporting information. Figure 8 displays breakthrough curves $P(\tilde{t}|\tilde{x})$ considering travel distances $\tilde{x} = 5$, 10, 25, and 50 from the injection location and provides a quantitative comparison between the reference DNS and the tSMM results. We note that the tSMM can reproduce the breakthrough curves across a wide range of distances and both Péclet numbers. This result shows that the trajectory-based upscaled model accurately predicts arrival times in a porous medium made of periodic unit cells displaying a disordered geometry and is in line with those obtained within simpler geometrical settings (Sund et al., 2017).

The comparison between tSMM and DNS marginal distribution of transverse locations $P(\tilde{y}|\tilde{x})$ is shown in Figure 9 for two selected distances from the injection ($\tilde{x} = 5$ and $\tilde{x} = 25$) and for both investigated Pe numbers.

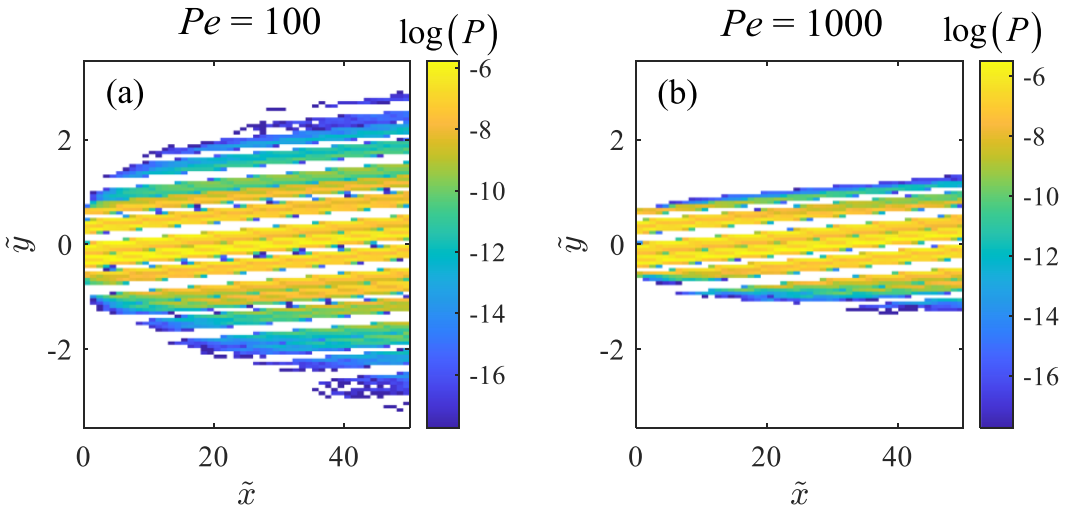

Figure 7. Marginal distribution $P(\tilde{x}, \tilde{y})$ for (a) $Pe = 100$ and (b) $Pe = 1{,}000$.

To compare the spreading of the particle plume over all Markov steps, we consider the standard deviation of distribution $P(\tilde{y}|\tilde{x})$ as a function of $\tilde{x}$ (see Figure 10).

Results obtained through the tSMM are in close agreement with those yielded by the DNS. We observe that the change in *Pe* has marked effects on transverse spreading of the solute, as has been previously observed in laboratory and numerical studies (Chiogna et al., 2010; Rolle et al., 2012). In particular, the standard deviation σ_y continuously increases as a function of the longitudinal distance traveled for $Pe = 100$. On the contrary, σ_y is approximately constant up to $\tilde{x} = 20$ for $Pe = 1{,}000$ and then starts increasing. This result implies that for such an advection-dominated situation we only observe significant transverse spreading after particles have traveled a distance of 20 cells. This result is due to the converging-diverging nature of advective streamlines in two-dimensional fields as can be detected in Figure 2. Such behaviors are certainly amplified with respect to a three-dimensional setting characterized by an analogous porosity. Yet the tSMM is able to predict these different dynamics based on the simulation of transport across a single two-dimensional unit cell. We are aware that behaviors observed in two-dimensional systems are often not transferable to three dimensions (Marafini et al., 2020), and we remark that the methodology can be extended to three dimensions, by relying on the same procedure described in section 2.2. We also emphasize that two-dimensional setups may be relevant in specific applications, e.g., the design or the modeling of experiments in microfluidic systems (e.g., Willingham et al., 2008).

Figures 11 shows the *HD* metric associated with results in Figures 8 and 9 as a function of the downstream location for $Pe = 100$ (red) and $Pe = 1{,}000$ (blue). We note that the *HD* metric is smaller than 5% in both cases

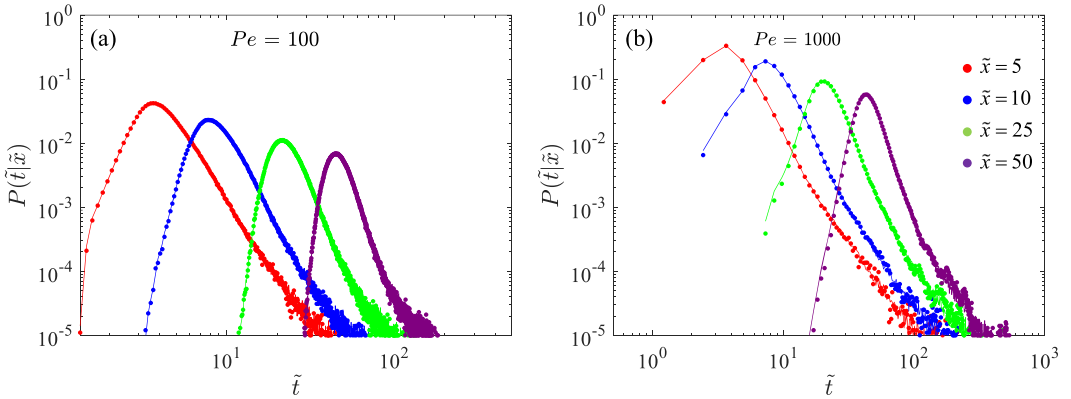

Figure 8. Breakthrough curves $P(\tilde{t}|\tilde{x})$ obtained at control planes located at distances $\tilde{x} = 5$, 10, 25, and 50 unit cells for (a) $Pe = 100$ and (b) $Pe = 1{,}000$. Symbols and lines represent the DNS and tSMM results, respectively.

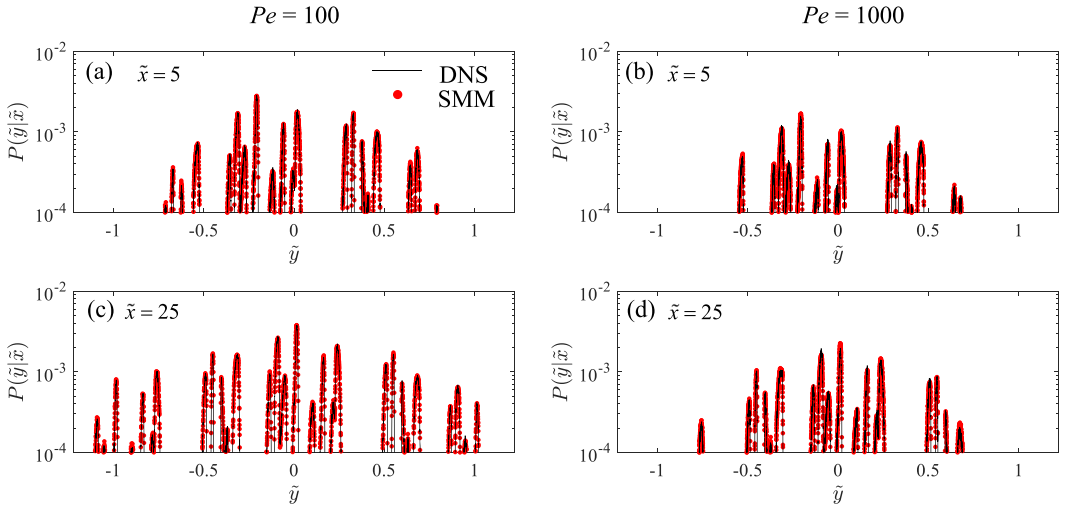

Figure 9. Comparison between the marginal distributions $P(\tilde{y}|\tilde{x})$ as given by direct numerical simulation (black lines) and tSMM (red dots) for $\tilde{x} = 5$ and (a) $Pe = 100$, (b) $Pe = 1{,}000$, for $\tilde{x} = 25$ and (c) $Pe = 100$ and (d) $Pe = 1{,}000$.

for both investigated Pe. This quantitatively demonstrates the high fidelity of the tSMM model in reproducing the DNS results.

3.2. Steady-State Plumes With First-Order Degradation

As a showcase application of the capabilities of the tSMM, we also evaluate the influence of a first-order reaction on pinching off the steady-state plume. Our choice relies on the fact that a linear reaction model is typically employed in a wide variety of situations including radioactive decay (Ciriello et al., 2013) and bioreactive systems (Cirpka & Valocchi, 2007). We assume in this application that the solute undergoes degradation following linear kinetics. This is accounted for in a straightforward manner in the tSMM framework. Starting from the conservative plume results (see Figure 7), for each particle we define the probability of reaction as $R_i(t, \lambda) = 1 - e^{-\lambda t}$, where λ is the kinetic degradation rate. Then we compare R_i with a random number, U_i, drawn from a standard uniform distribution. If $U_i \geqslant P_i$, no reaction occurs, while if $U_i < P_i$, the particle is removed from the system. In our examples λ is chosen based on obtaining specific values of Damkhöler numbers, $Da = \frac{\ell_s^2 \lambda}{D}$.

We compute marginal distributions $P(\tilde{x}, \tilde{y})$ to represent the steady-state plume for this reactive scenario. The results obtained for $Da = 1$ and 5 (corresponding to $\lambda = 0.1$ and $0.5\,\mathrm{s}^{-1}$) and $Pe = 100$ are depicted in Figures 12a and 12b while Figures 12c and 12d show the case associated with $Da = 5$ and 10 (corresponding to $\lambda = 0.5$ and $1\,\mathrm{s}^{-1}$) and $Pe = 1{,}000$. These results portray the ability of our proposed tSMM to predict transport

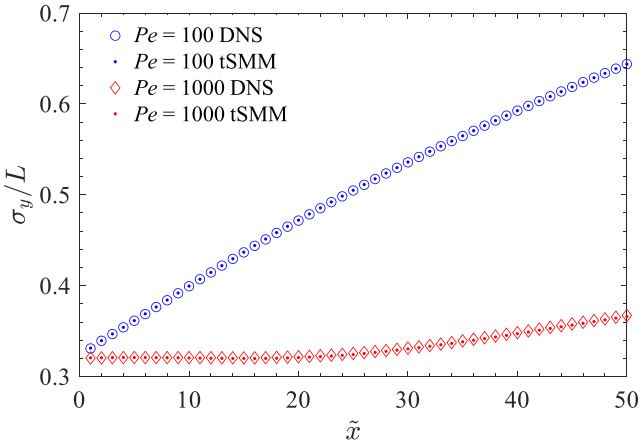

Figure 10. Comparison of the standard deviation, σ_y, of the distribution $P(\tilde{y}|\tilde{x})$ for the DNS and tSMM as a function of $\tilde{x}$.

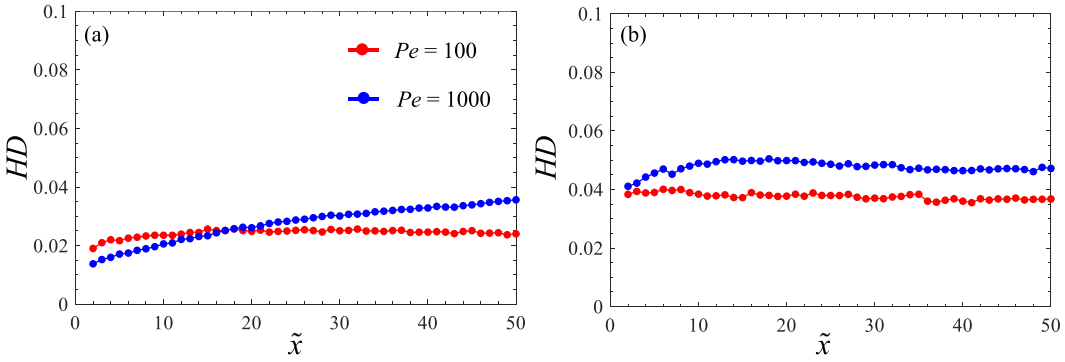

Figure 11. (a) $HD[P_{DNS}(\tilde{t}|\tilde{x}); P_{tSMM}(\tilde{t}|\tilde{x})]$ and (b) $HD[P_{DNS}(\tilde{y}|\tilde{x}); P_{tSMM}(\tilde{y}|\tilde{x})]$ as a function of the downstream location $\tilde{x}$ for $Pe = 100$ (red) and $Pe = 1{,}000$ (blue).

in longitudinal and transverse direction while also accounting for a reactive solute undergoing a first order reaction process. Note that the results are obtained at negligible additional computational cost with respect to the unsteady state, conservative, transport simulations.

3.3. Error Analysis

To provide a quantitative description of the influence of parameters N_B and dt on the accuracy of the proposed SMM, we evaluate $HD[F_1, F_2]$, see Equation 7, choosing as F_1 and F_2 the marginal distributions of

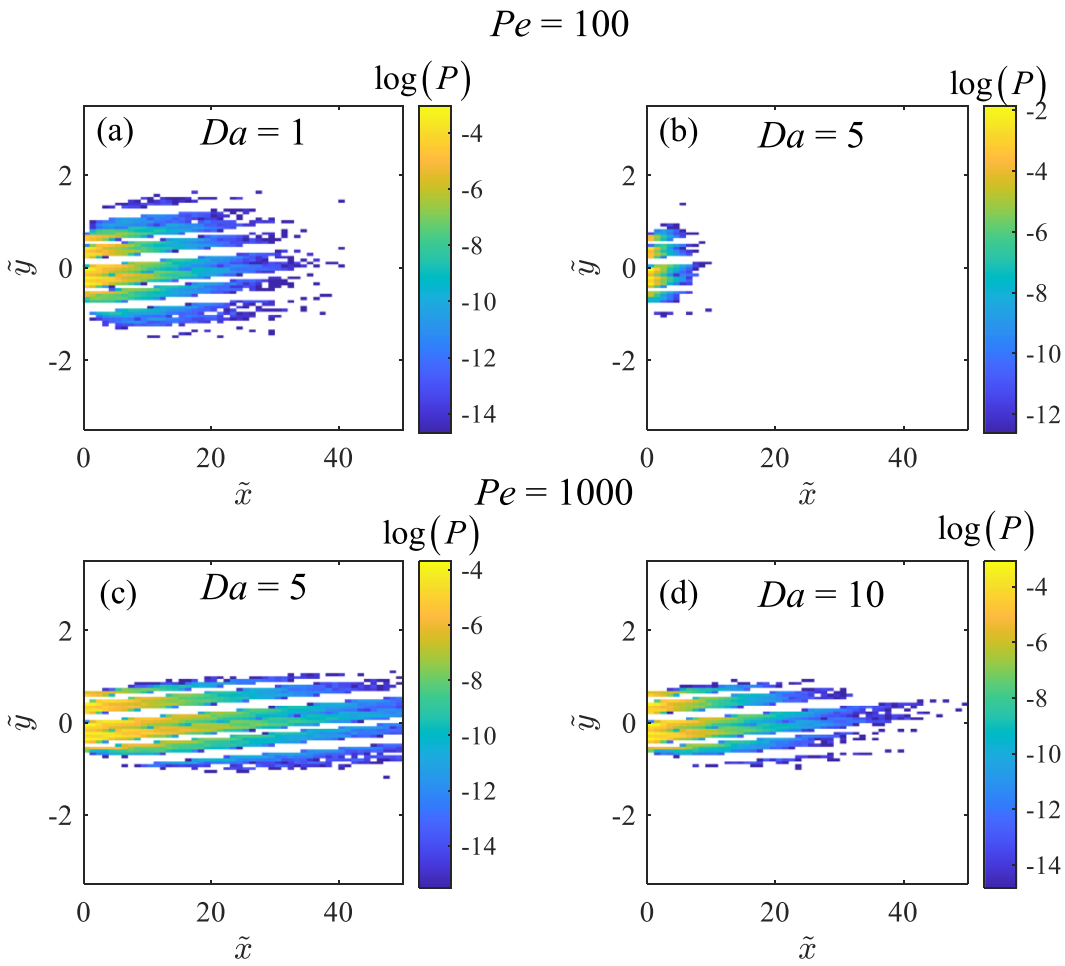

Figure 12. Marginal distribution $P(\tilde{x}, \tilde{y})$ for a reactive contaminant undergoing a degradation following a linear kinetics for $Pe = 100$ (a) $Da = 1$, (b) $Da = 5$, and $Pe = 1{,}000$ (c) $Da = 5$, (d) $Da = 10$.

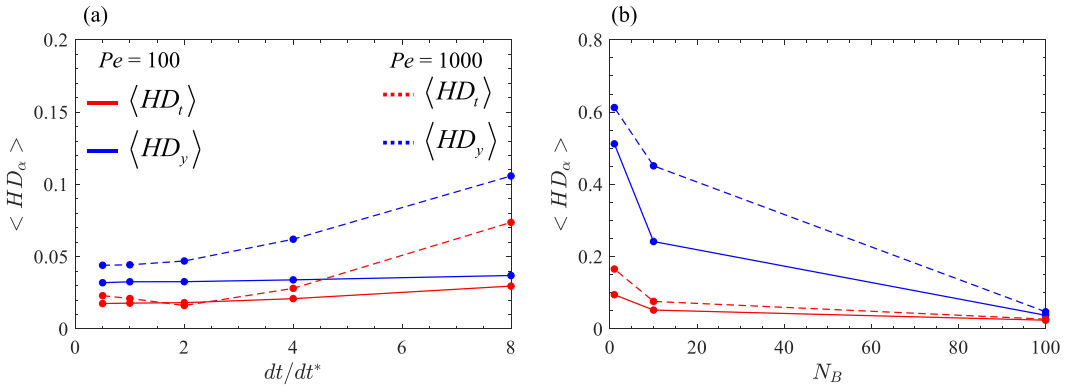

Figure 13. $\langle HD_\alpha \rangle$ for $Pe = 100$ and $Pe = 1{,}000$ as a function of the Markov step number (cell number) for different dt and numbers of bins N_B employed in the parameterization step.

travel times, $P(\tilde{t}|\tilde{x})$, or transverse positions, $P(\tilde{y}|\tilde{x})$, conditional to a given downstream location $\tilde{x}$ from the injection point, evaluated with DNS and tSMM, respectively. Note that the time step is kept constant and equal to dt^* in the DNS, while we consider in the following different values for the simulation of the trajectories employed to parameterize the tSMM, To simplify the notation, we introduce here the following indicators:

$$HD_t = HD[P_{DNS}(\tilde{t}|\tilde{x}); P_{SMM}(\tilde{t}|\tilde{x})] \tag{8}$$

$$HD_y = HD[P_{DNS}(\tilde{y}|\tilde{x}); P_{SMM}(\tilde{y}|\tilde{x})] \tag{9}$$

to assess the model errors. The analysis is performed considering both $Pe = 100$ and $Pe = 1{,}000$ and considering different values of N_B and dt for the parameterization of the tSMM, while, as mentioned above, in the reference DNS the dt is constant and equal to dt^*. In order to provide an overall assessment of the impact of parameters dt and N_B, we focus on the average of HD_α (with $\alpha = t, y$) across all 50 investigated Markov steps (the averaging operator is denoted by the symbol $\langle\cdot\rangle$). Figures 13a and 13b show $\langle HD_t \rangle$ and $\langle HD_y \rangle$ as a function of dt/dt^* and N_B, respectively. Continuous lines correspond to $Pe = 100$, while dashed lines depict results associated with $Pe = 1{,}000$. Red and blue colors are related to arrival time and transverse location distributions, respectively. Note that for $Pe = 100$ both $\langle HD_t \rangle$ and $\langle HD_y \rangle$ are not very sensitive to the choice of parameter dt (see Figure 13a). On the contrary for $Pe = 1{,}000$ we observe a sharp increase of $\langle HD_t \rangle$ and $\langle HD_y \rangle$ for $dt > 2dt^*$. This is probably due to the fact that advective particle displacements depend linearly on dt, as opposed to the diffusive ones which scale with $dt^{0.5}$. The variation of $\langle HD_t \rangle$ and $\langle HD_y \rangle$ as a function of N_B is displayed in Figure 13b for the two investigated Pe numbers. These results show that the quality of model predictions deteriorates for decreasing number of bins associated with the tSMM parameterization. Note that $N_B = 1$ corresponds to considering the particle trajectories as totally uncorrelated across successive Markov steps, while setting $N_B > 1$ in the tSMM parameterization allows consideration of correlation between particle trajectories belonging to the same bin. We note that considering uncorrelated particle trajectories does not provide good agreement between DNS and tSMM distributions, as indicated by high values of the HD_α metrics. Also in this case correlation effects at a fixed downstream distance become stronger as Péclet number increases, in line with the results of previous studies (Bolster et al., 2014; Sherman et al., 2019).

4. Discussion and Conclusions

Our study proposes a methodology for upscaling solute plumes in periodic porous media through a tSMM. We extend the work of Sund et al. (2017) to the case of a multidimensional unsteady solute transport and exemplify our approach considering a two-dimensional porous medium with a disordered geometry. Our framework is based on the simulation of advection-diffusion random walk particle trajectories across a single periodic flow cell with the aim of predicting transport over a much larger scale. In particular, our analysis explicitly includes the evaluation of the joint space-time probability distributions associated with solute

plumes providing an efficient and accurate representation of both transient and steady-state transport in porous media for different *Pe* numbers. Our work leads to the following major conclusions:

1. From a comparison with high-resolution DNSs we show that the proposed tSMM accurately predicts spatial and temporal distributions of a conservative solute plume using information collected from a single cell simulation. The current framework is not restricted to a simplified geometry setting or a particular flow condition but can be employed to accurately predict multidimensional transport in a disordered two-dimensional pore space once the flow field has been evaluated. Note that in principle our methodology can be used with different type of initial injection condition, for example, flux-weighted or uniformly distributed, pulse or continuous injection, and can be extended to a three-dimensional setup.
2. Our model is able to predict different transport dynamics, particularly regarding the influence of *Pe* on transverse plume spreading. Our results are in line with previous laboratory and numerical studies (Chiogna et al., 2010; Rolle et al., 2012). In particular, the change in *Pe*, due to a change in the diffusion coefficient of the compound, had marked effects on transverse spreading of the solute and this is well captured by our upscaling approach.
3. Particle trajectories and associated travel times, which were simulated with the proposed tSMM to predict conservative transport, can be naturally extended to simulate reactive transport processes with negligible additional computational cost. As an example, in this work we analyze the influence of a first-order kinetic reaction on a steady-state plume. To do so, our model has been coupled with a probabilistic representation of a linear degradation reaction and applied for several *Da* numbers. Note that the methodology is already fully compatible with the analysis of other types of reactions (e.g., sorption/desorption) as was shown by Sherman et al. (2019) for an idealized benchmark problem.
4. The effect of tSMM parameterization (in particular the parameters dt and N_B) was studied for the two analyzed *Pe*. As expected, the difference between tSMM and DNS distribution both in space and time increases with increasing dt and decreasing N_B, respectively. A marked effect of parameterization was observed for $Pe = 1{,}000$ with respect to $Pe = 100$ due to fact that (i) the contribution of the advective transport, which increases with *Pe*, is more affected by the choice of dt employed in the tSMM parameterizazion and (ii) the relevance of particle trajectory correlation increases with *Pe*.

For all the above points the simulation time needed for the tSMM is negligible if compared to the one required for high-resolution DNS. This is one of the great advantages of the proposed tSMM which allows predictions of multidimensional transport across large distances (for both conservative and reactive solutes) without the burden of excessive computational resources. Note that, in its current form, the model can be applied to a spatially periodic domain. This restriction is similar to the fact that solving a closure problem on a periodic unit cell is required for many well-established upscaling procedures. At the same time, broadening the scenarios of interest, for example, extending the methodology to upscaling transport of a conservative and/or reactive solute in a disordered nonperiodic porous domain, as well as to interpret laboratory and/or field-scale observations, would constitute additional elements of interest which are compatible with the approach we rest upon. This will hopefully now be possible after the model has been formulated and tested in a synthetic and controlled scenario such as the one presented here. A first attempt in the direction of nonperiodic media is available in (Sherman, Bianchi Janetti, et al., 2020; Sherman, Hyman, et al., 2020) who obtain promising results which can be built on in the context of future investigations.

Data Availability Statement

Data sets for this research are available online (at https://data.mendeley.com/datasets/rzg53tn963/1).

Acknowledgments
D. B. and T. S. were supported by, or in part by, the U.S. Army Research Office under Contract/Grant number W911NF-18-1-0338 and by the National Science Foundation under award EAR-1951677.

References

Auriault, J.-L., Moyne, C., & Souto, H. P. A. (2010). On the asymmetry of the dispersion tensor in porous media. *Transport in Porous Media*, *85*(3), 771–783. https://doi.org/10.1007/s11242-010-9591-y

Berkowitz, B., Cortis, A., Dentz, M., & Scher, H. (2006). Modeling non-Fickian transport in geological formations as a continuous time random walk. *Reviews of Geophysics*, *44*, RG2003. https://doi.org/10.1029/2005RG000178

Bolster, D., Méheust, Y., Le Borgne, T., Bouquain, J., & Davy, P. (2014). Modeling preasymptotic transport in flows with significant inertial and trapping effects—The importance of velocity correlations and a spatial Markov model. *Advances Water Resources*, *70*, 89–103. https://doi.org/10.1016/j.advwatres.2014.04.014

Cheng, A. H.-D., & Bear, J. (2016). *Modeling groundwater flow and contaminant transport*. Dordrecht: Springer Publishing Company.

Chiogna, G., Eberhardt, C., Grathwohl, P., Cirpka, O. A., & Rolle, M. (2010). Evidence of compound-dependent hydrodynamic and mechanical transverse dispersion by multitracer laboratory experiments. *Environmental Science and Technology*, *44*(2), 688–693. https://doi.org/10.1021/es9023964

Ciriello, V., Di Federico, V., Riva, M., Cadini, F., De Sanctis, J., Zio, E., & Guadagnini, A. (2013). Polynomial chaos expansion for global sensitivity analysis applied to a model of radionuclide migration in a randomly heterogeneous aquifer. *Stochastic Environmental Research and Risk Assessment*, *27*, 945–954. https://doi.org/10.1007/s00477-012-0616-7

Cirpka, O. A., & Valocchi, A. J. (2007). Two-dimensional concentration distribution for mixing-controlled bioreactive transport in steady state. *Advances in Water Resources*, *30*(6–7), 1668–1679. https://doi.org/10.1016/j.advwatres.2006.05.022

Davit, Y., Wood, B. D., Debenest, G., & Quintard, M. (2012). Correspondence between one-and two-equation models for solute transport in two-region heterogeneous porous media. *Transport in Porous Media*, *95*(1), 213–238. https://doi.org/10.1007/s11242-012-0040-y

Gebäck, T., & Heintz, A. (2019). A pore scale model for osmotic flow: Homogenization and lattice boltzmann simulations. *Transport in Porous Media*, *126*(1), 161–176. https://doi.org/10.1007/s11242-017-0975-0

Hellinger, E. (1909). Neue begrundung der theorie quadratischer formen von unendlichvielen veränderlichen. *Journal Für Die Reine Und Angewandte Mathematik*, *1909*, 210–271. https://doi.org/10.1515/crll.1909.136.210

Hyman, J. D., & Winter, C. L. (2014). Stochastic generation of explicit pore structures by thresholding Gaussian random fields. *Journal of Computational Physics*, *277*, 16–31. https://doi.org/10.1016/j.jcp.2014.07.046

Kang, P. K., Anna, P., Nunes, J. P., Bijeljic, B., Blunt, M. J., & Juanes, R. (2014). Pore-scale intermittent velocity structure underpinning anomalous transport through 3-D porous media. *Geophysical Research Letters*, *41*, 6184–6190. https://doi.org/10.1002/2014GL061475

Kim, H., Bae, J., & Choi, D. (2013). An analysis for a molten carbonate fuel cell of complex geometry using three-dimensional transport equations with electrochemical reactions. *International Journal of Hydrogen Energy*, *38*(11), 4782–4791. https://doi.org/10.1016/j.ijhydene.2013.01.061

Koch, J., & Nowak, W. (2014). A method for implementing Dirichlet and third-type boundary conditions in PTRW simulations. *Water Resources Research*, *50*, 1374–1395. https://doi.org/10.1002/2013WR013796

Kullback, S., & Leibler, R. A. (1951). On information and sufficiency. *Annals of Mathematical Statistics*, *22*(1), 79–86. https://doi.org/10.1214/aoms/1177729694

Le Borgne, T., Bolster, D., Dentz, M., Anna, P., & Tartakovsky, A. (2011). Effective pore-scale dispersion upscaling with a correlated continuous time random walk approach. *Water Resources Research*, *47*, W12538. https://doi.org/10.1029/2011WR010457

Marafini, E., La Rocca, M., Fiori, A., Battiato, I., & Prestininzi, P. (2020). Suitability of 2D modelling to evaluate flow properties in 3D porous media. *Transport in Porous Media*, *134*(2), 315–329. https://doi.org/10.1007/s11242-020-01447-4

Most, S., Bolster, D., Bijeljic, B., & Nowak, W. (2019). Trajectories as training images to simulate advective-diffusive, non-fickian transport. *Water Resources Research*, *55*, 3465–3480. https://doi.org/10.1029/2018WR023552

Municchi, F., & Icardi, M. (2020). Macroscopic models for filtration and heterogeneous reactions in porous media. *Advances in Water Resources*, *141*, 103605. https://doi.org/10.1016/j.advwatres.2020.103605

Muniruzzaman, M., & Rolle, M. (2015). Impact of multicomponent ionic transport on pH fronts propagation in saturated porous media. *Water Resources Research*, *51*, 6739–6755. https://doi.org/10.1002/2015WR017134

OpenCFD Limited (2017). OpenFOAM The Open Source CFD Toolbox, user guide version v1712. https://www.openfoam.com/, Accessed: 2019-09-29.

Porta, G. M., Ceriotti, G., & Thovert, J.-F. (2016). Comparative assessment of continuum-scale models of bimolecular reactive transport in porous media under pre-asymptotic conditions. *Journal of Contaminant Hydrology*, *185*, 1–13. https://doi.org/10.1016/j.jconhyd.2015.12.003

Pride, S. R., Vasco, D. W., Flekkoy, E. G., & Holtzman, R. (2017). Dispersive transport and symmetry of the dispersion tensor in porous media. *Physical Review E*, *95*(4), 043103. https://doi.org/10.1103/PhysRevE.95.043103

Puyguiraud, A., Gouze, P., & Dentz, M. (2019). Stochastic dynamics of Lagrangian pore-scale velocities in three-dimensional porous media. *Water Resources Research*, *55*, 1196–1217. https://doi.org/10.1029/2018WR023702

Rolle, M., Hochstetler, D., Chiogna, G., Kitanidis, P. K., & Grathwohl, P. (2012). Experimental investigation and pore-scale modeling interpretation of compound-specific transverse dispersion in porous media. *Transport in Porous Media*, *93*(3), 347–362. https://doi.org/10.1016/j.advwatres.2020.103574

Russian, A., Dentz, M., & Gouze, P. (2016). Time domain random walks for hydrodynamic transport in heterogeneous media. *Water Resources Research*, *52*, 3309–3323. https://doi.org/10.1002/2015WR018511

Salles, J., Thovert, J.-F., Delannay, R., Prevors, L., Auriault, J.-L., & Adler, P. M. (1992). Taylor dispersion in porous media. Determination of the dispersion tensor. *Physics of Fluids A*, *5*(10), 2348–2376. https://doi.org/10.1063/1.858751

Scheidegger, A. E. (1954). Statistical hydrodynamics in porous media. *Journal of Applied Physics*, *25*(8), 994–1001. https://doi.org/10.1063/1.1721815

Schmuck, M., & Berg, P. (2014). Effective macroscopic equations for species transport and reactions in porous catalyst layers. *Journal of the Electrochemical Society*, *161*(8), E3323–E3327. https://doi.org/10.1149/2.037408jes

Sherman, T., Bianchi Janetti, E., Raymond Guédon, G., Porta, G., & Bolster, D. (2020). Upscaling transport of a sorbing solute in disordered non periodic porous domains. *Advances in Water Resources*, *139*, 103574. https://doi.org/10.1016/j.advwatres.2020.103574

Sherman, T., Foster, A., Bolster, D., & Singha, K. (2018). Predicting downstream concentration histories from upstream data in column experiments. *Water Resources Research*, *54*, 9684–9694. https://doi.org/10.1029/2018WR023420

Sherman, T., Hyman, J., Dentz, M., & Bolster, D. (2020). Characterizing the influence of fracture density on network scale transport. *Journal of Geophysical Research: Solid Earth*, *125*, e2019JB018547. https://doi.org/10.1029/2019JB018547

Sherman, T., Paster, A., Porta, G., & Bolster, D. (2019). A spatial Markov model for upscaling transport of adsorbing-desorbing solutes. *Journal of contaminant hydrology*, *222*, 31–40. https://doi.org/10.1016/j.jconhyd.2019.02.003

Smolarkiewicz, P. K., & Winter, C. L. (2010). Pores resolving simulation of Darcy flows. *Journal of Computational Physics*, *229*(9), 3121–3133. https://doi.org/10.1016/j.jcp.2009.12.031

Sole-Mari, G., Bolster, D., Fernandez-Garcia, D., & Sanchez-Vila, X. (2019). Particle density estimation with grid-projected and boundary-corrected adaptive. *Advances in water resources*, *131*, 103382. https://doi.org/10.1016/j.advwatres.2019.103382

Sund, N. L., Porta, G. M., & Bolster, D. (2017). Upscaling of dilution and mixing using a trajectory based spatial Markov random walk model in a periodic flow domain. *Advances in Water Resources*, *103*, 76–85.

Tang, Y., Werth, C. J., Sanford, R. A., Singh, R., Michelson, K., Nobu, M., et al. (2015). Immobilization of selenite via two parallel pathways during in situ bioremediation. *Environmental Science and Technology*, *49*(7), 4543–4550. https://doi.org/10.1021/es506107r

Valdés-Parada, F. J., Lasseux, D., & Bellet, F. (2016). A new formulation of the dispersion tensor in homogeneous porous media. *Advances in Water Resources*, *90*, 70–82. https://doi.org/10.1016/j.advwatres.2016.02.012

Willingham, T. W., Werth, C. J., & Valocchi, A. J. (2008). Evaluation of the effects of porous media structure on mixing-controlled reactions using pore-scale modeling and micromodel experiments. *Environmental Science and Technology*, *42*(9), 3185–3193. https://doi.org/10.1021/es7022835

Wood, B. D., & Valdés-Parada, F. J. (2013). Volume averaging: Local and nonlocal closures using a Green's function approach. *Advances in Water Resources*, *51*, 139–167. https://doi.org/10.1016/j.advwatres.2012.06.008

Wright, E., Sund, N., Richter, D., Porta, G., & Bolster, D. (2019). Upscaling mixing in highly heterogeneous porous media via a spatial Markov model. *Water*, *11*(1), 53. https://doi.org/10.3390/w11010053

Ye, Y., Chiogna, G., Cirpka, O. A., Grathwohl, P., & Rolle, M. (2016). Experimental investigation of transverse mixing in porous media under helical flow conditions. *Physical Review E*, *94*(1), 013113. https://doi.org/10.1103/PhysRevE.94.013113